Available online at www.sciencedirect.com
ScienceDirect
International Journal of Heat and Mass Transfer 51 (2008) 4797–4810
International Journal of HEAT and MASS TRANSFER
www.elsevier.com/locate/ijhmt

Shear-driven flows of locally heated liquid films

Elizaveta Ya. Gatapova [a,b,*], Oleg A. Kabov [a,b,c]

[a] Institute of Thermophysics, Russian Academy of Sciences, 630090 Novosibirsk, Russia
[b] Heat Transfer International Research Institute of ULB and IT RAS, Brussels, Belgium
[c] Microgravity Research Centre, Université Libré dé Bruxelles, Brussels, Belgium

Received 30 July 2007; received in revised form 21 October 2007
Available online 28 May 2008

Abstract

This paper considers the flow of a liquid film sheared by gas flow in a channel with a heater placed at the bottom wall. A one-sided 2D model is considered for weakly heated films. The heat and mass transfer problem is also investigated in the framework of a two-sided model. The exact solution to the problem of heat transfer is obtained for a linear velocity profile. The double effect of Marangoni forces is demonstrated by the formation of a liquid bump in the vicinity of the heater's upper edge and film thinning in the vicinity of the lower edge. The criterion determining the occurrence of "ripples" on the film surface upstream from the bump is found. Numerical analysis reveals that evaporation dramatically changes the temperature distribution, and hence, thermocapillary forces on the gas–liquid interface. All transport phenomena (convection to liquid and gas, evaporation) are found to be important for relatively thin films, and the thermal entry length is a determining factor for heaters of finite length. The thermal entry length depends on film thickness, which can be regulated by gas flow rate or channel height. The influence of the convective heat transfer mechanism is much more prominent for relatively high values of the liquid Reynolds number. The liquid–gas interface Biot number is shown to be a sectional-hyperbolic function of a longitudinal axis variable. Some qualitative and quantitative comparisons with experimental results are presented.
© 2008 Elsevier Ltd. All rights reserved.

Keywords: Liquid film; Gas flow; Non-uniform heating; Marangoni force; Evaporation; Micro/minichannels

1. Introduction

Shear-induced flows of liquid films, caused by different shear forces, are important for several technological innovations for ground and space applications. This paper investigates liquid films driven by the action of gas flow in a microchannel with a local heater. A variety of important phenomena can be observed in this physical process, such as the formation of waves [1,2], capillary, solutocapillary and thermocapillary patterns [3,4], and microscopic peculiarities [5,6]. One of the promising applications of shear-driven liquid films is the cooling of microelectronic components [7,8]. The heat flux densities in these components may be as high as 300 W/cm^2 [9]. The efficient devices used to cool microelectronics are based on evaporation. Thin annular liquid films may provide very high heat transfer intensity, especially in the micro region near the contact line [5,10].

Thermocapillary convection of a gravity-driven liquid film on a heated substrate has been extensively studied over the last several decades. Several theoretical models have been proposed that are capable of describing a gravity-driven liquid film with local heating at the substrate [11–13]. Frank [14] performed a direct three-dimensional non-linear simulation of the flows in a locally heated film using the particle method, and the numerical results were in agreement with the experimental data. A review of most results concerning the effect of non-uniform heating on film flow can be found in the introduction of [15]. However, non-uniform heating and Marangoni effects have been only partially understood for shear-driven liquid film flows [16,17],

* Corresponding author. Address: Institute of Thermophysics, Russian Academy of Sciences, 630090 Novosibirsk, Russia. Tel.: +7 383 3165137; fax: +7 383 3308480.
E-mail address: gatapova@itp.nsc.ru (E.Ya. Gatapova).

0017-9310/$ - see front matter © 2008 Elsevier Ltd. All rights reserved.
doi:10.1016/j.ijheatmasstransfer.2008.02.038

Nomenclature

a	thermal diffusivity coefficient
B	channel width
Bi	Biot number
Bo	Bond number
Bo^*	associated Bond number
C	concentration (kg/m^3)
C^*	equilibrium concentration at the surface of evaporating liquid (kg/m^3)
C_0, C_1	equilibrium concentration coefficients
$\overline{C}$	analogue of capillary number
c_p	specific heat capacity (J/kg K)
D	diffusion coefficient (m^2/s)
$F(X)$	fundamental solution
$f(X)$	function
g	gravity acceleration
H	channel height
h	film thickness
$\bar{h}$	dimensionless film thickness
h_1	dimensionless linearized film thickness
L	heater length
l_σ	capillary length
M	molar mass
m	mass concentration
Ma	Marangoni number
n	natural number
P	dimensionless pressure
p	pressure
p_0, p_1	vapor partial pressure at T_0, T_1
$\bar{p}$	characteristic pressure
Pe	Peclet number
Pr	Prandtl number
Q	specific flow rate (m^2/s)
q	heat flux density (W/cm^2)
q_0	heat flux density on the heating element (W/cm^2)
R	universal gas constant
r	heat of vaporization (J/kg)
Re	Reynolds number
T	temperature (K, °C)
ΔT	characteristic temperature drop (K, °C)
U, V	dimensionless velocity components
u, v	velocity components in the x and y axes
$\bar{u}, \bar{v}$	mean velocity components
X, Y	dimensionless Cartesian coordinates
x, y	Cartesian coordinates
x_m	point of the onset of heat flux reduction

Greek symbols

α	heat transfer coefficient (W/m^2 K)
Γ	specific mass flow rate of liquid (kg/ms)
Γ_e	specific mass flow rate of evaporated liquid (kg/ms)
ε	ratio of linear film scales
γ	dimensionless mass flow rate
θ	dimensionless temperature
$\bar{\theta}$	dimensionless film surface temperature
λ	thermal conductivity coefficient
μ	dynamic viscosity
$\eta(X)$	function $= \chi(X) - \chi(X-1)$
ρ	density
σ	liquid surface tension (N/m)
σ_T	surface tension temperature dependent coefficient (N/m K)
τ	shear stress at the interface
T	dimensionless shear stress
φ	inclination angle of the channel
$\chi(X)$	Heaviside function

Subscripts and superscripts

0	initial flow parameters specified at $T = T_0$
a	air
g	gas phase
I	gas–liquid interface
max	maximum
v	vapor
W	bottom wall

and the influence of the gas phase on the interfacial phenomena remains a challenging issue for modeling.

Most of the papers dealing with the interaction between evaporation and thermocapillary effects assume that the liquid is only in contact with its own vapor [18]. While experimental and theoretical investigations show that the presence of a non-condensable component in the vapor phase strongly leads to surface-tension-driven instability of an evaporating liquid layer [19]. One of the examples is the ridges and dendritic structure formation due to evaporative instability in climbing films reported in [20]. Rosskamp et al. [21] conducted experimental investigations of evaporating shear-driven liquid wall films in hot turbulent air flow. Mathematical models describing the evaporation of liquids more often than not deal with the evaporation of a liquid film in an open space, such as a flat plate in air [22]. The evaporation of a falling liquid film on an inclined plate in a laminar stream of humid air has been studied numerically by Mezaache and Daguenet [23]. They showed that the enthalpy diffusion term can be neglected in the heat equation for the gas phase. The heat and mass transfer involved in the evaporation of a water falling film in a closed rectangular cavity was recently studied numerically and experimentally by the authors of [24]. To our knowledge, most theoretical works concerning two-phase flow have used a 2D formulation. It is worth noting that Lakehal et al. [25] present the recent trends in the development of prediction methods for the direct numerical simu-

lation of multiphase flows based on the one-fluid formalism coupled with various interface tracking algorithms.

Contrary to gravity-driven isothermal liquid films, shear-driven films are less likely to breakdown [26], and yet it is well known that the Marangoni effect has a significant influence on heat transfer intensity and may lead to film rupture [27,28]. This provides a way to prevent and control a hot dry patch formation by the shear stress induced by gas flow. It is quite evident that the combined effects of evaporation, thermocapillarity, and gas dynamics, as well as the formation of microscopic adsorbed film, result in a number of complicated issues and have not yet been studied systematically. The aim of the present work is to investigate the film deformations due to Marangoni forces and to study the effect of evaporation on the enhancement of heat transfer from a local heater for a shear-driven liquid film in a microchannel.

We consider two types of models for the heated shear-driven liquid film. First of them is a one-sided model in the framework of lubrication approximation when the evaporation is negligible. The lubrication theory or long-wave theory has been used in the analysis of many type of thin liquid film flow [29] arising in a number of industrial applications including flow of liquids over a heated solid surfaces. Most of works in this type of studying of a heated liquid films assume that the convective terms in the energy equation are negligible and this leads to just one equation of Benney type for the film thickness [12,29]. However, for the thermocapillary instability problem of nonuniformly heated gravity-driven liquid film (see the experiments [4,11]) clearly indicate that the temperature field is convected downstream and is very different from the solution of simple heat conduction equation. In fact, the Peclet number in the experiments [4] is O(1) or even larger. The difference of our model proposed here from the classical models for nonisothermal liquids in lubrication approximation [29] is that the convective terms in energy equation is incorporated into the model and coupled to the equation for the film thickness. So that the model is valid for Peclet number O(1) or larger. The second model is developed to study the evaporation effect on heat transfer in the framework of two-sided model for shear-driven liquid films. The model includes the energy equations for liquid and gas phases, and the convection–diffusion equation with the appropriate boundary conditions. All the equations consider the Peclet numbers O(1) or larger and include the convective terms and expected to be valid for laminar flows in both the liquid and gas phases (for moderate Reynolds numbers).

The paper is organized as follows: the problem is described in Section 2, and a one-sided 2D model is considered for weakly heated films in Section 3, some results of this section has been published in Letter [16]. The problems of heat transfer and thermocapillary deformation are discussed; evaporation is neglected, with the heat transfer to the gas phase approximately specified by a constant Biot number. Section 4 analyzes the evaporation effect on heat transfer; a quantitative comparison with the experimental data is made; and finally, the key findings are summarized in Section 5.

2. Description of the problem

Consider a channel with a rectangular cross section, the height of which, H, is much less than its width, B. A viscous incompressible liquid film flows under the action of gas flow and under the action of gravity when the channel is inclined at an angle φ with respect to the horizontal plane, as shown in Fig. 1. Suppose there is a local heater on the bottom wall.

Experimental investigations of isothermal shear-driven liquid films indicate that for small liquid and gas flow rates, the film surface is smooth throughout the length of the channel [30]. Furthermore, the initial section of smooth film exists even for higher gas/liquid flow rates. Accordingly, this theoretical investigation is considered in the framework of flow regimes without waves with velocity profiles for laminar co-current parallel streams, or Couette flow with a nonzero pressure drop:

$$u(y) = \frac{1}{\mu}\left(\left(\rho g \sin\varphi - \frac{\partial p}{\partial x}\right)\left(h_0 y - \frac{y^2}{2}\right) + \tau y\right), \tag{1}$$

$$u_g(y) = \frac{1}{\mu_g}\left(\left(\rho_g g \sin\varphi - \frac{\partial p}{\partial x}\right) \times \left(h_0(y-H) - \frac{y^2 - H^2}{2}\right) + \tau(y-H)\right). \tag{2}$$

For a given channel height and liquid and gas Reynolds numbers, velocity profiles, film thickness, tangential stress and the drop in pressure can be found by solving the problem of joint motion of isothermal non-deformable liquid film and gas flow in the channel:

$$\tau = 2\frac{H-h_0}{Hh_0^2}\left[\mu Q - (\rho-\rho_g)g\sin\varphi\frac{h_0^3}{3} - \mu_g Q_g \frac{h_0^3}{(H-h_0)^3}\right]$$

$$\frac{\partial p}{\partial x} = \rho_g g\sin\varphi - \mu_g Q_g \frac{3}{(H-h_0)^3} - \frac{3}{Hh_0^2}\mu Q + \frac{h_0}{H}(\rho-\rho_g)g\sin\varphi + \frac{3}{H}\mu_g Q_g \frac{h_0}{(H-h_0)^3}$$

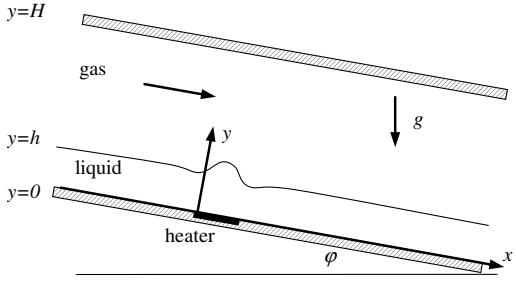

Fig. 1. Sketch of shear-driven liquid film flow in a microchannel with a local heater.

Initial film thickness, h_0, is found to be the root of the polynomial of degree 5. Here and below initial means the data for the reference state (i.e. when there is no evaporation, heating and waves). The results for h_0, τ, u, u_g from this Section are used in Sections 3 and 4.

3. Films under weak thermal effects

3.1. Formulation

In this section we consider the flow of shear-driven liquid films under relatively small heat flux densities. This means that $Ma \ll 1$ and the evaporation effect can be neglected, with the heat transfer to gas approximately specified by a constant Biot number. We will not discuss the temperature dependence of the liquid viscosity [31,14] since we consider only cases of weak heating in this section. The dynamic influence of gas flow will be modelled by a constant shear stress τ, found from the problem of joint motion of isothermal non-deformable liquid film and gas flow in the channel (Section 2).

Consider a stationary two-dimensional flow of the heated liquid film sheared by gas flow. We introduce the non-dimensional variables:

$$X = x/L, \quad Y = y/h_0, \quad U = u/\bar{u}, \quad V = v/\bar{v}, \quad \bar{h} = h/h_0, \quad \mathrm{T} = \tau/\tau_0, \quad \theta = (T - T_0)/\Delta T, \quad \bar{\theta} = (T(x,h) - T_0)/\Delta T, \quad \theta_g = (T_g - T_0)/\Delta T, \quad P = (p - p_g)/\bar{p},$$

where $\bar{u} = \frac{1}{\mu}\left(\rho g \sin\varphi \frac{h_0^2}{3} + \frac{\tau h_0}{2}\right)$, $\bar{v} = \varepsilon\bar{u}, \varepsilon = h_0/L$, $\tau_0 = \mu\bar{u}/h_0$, $\bar{p} = \mu\bar{u}/\varepsilon h_0$, and $\Delta T = q_0 L/c_p\Gamma$ characterizes the variation in temperature along the heater.

For a linear velocity profile in the film, the average velocity of the liquid film is expressed in terms of the tangential stress as $\bar{u} = \tau h_0/2\mu$, so the non-dimensional tangential stress becomes $\mathrm{T} = \tau/\tau_0 = 2$. Physically, such situations take place if the channel is normally oriented to any acting body force. For example, this applies in a horizontally placed channel in a gravitational field, or under the complete absence of a body force as would occur in a non-rotating space vehicle (microgravity conditions).

Ignoring the terms of the order ε^2 and higher, and considering inertial terms to be negligible $\varepsilon Re = \mathrm{O}(\varepsilon^2)$, (assuming the lubrication approximation is valid), we obtain the non-dimensional formulation. The dimensionless governing equations are

$$\varepsilon U_{YY} - \varepsilon P_X + \frac{\rho g h_0}{\bar{p}} \sin\varphi = 0, \tag{3}$$

$$-P_Y - \frac{\rho g h_0}{\bar{p}} \cos\varphi = 0, \tag{4}$$

$$U_X + V_Y = 0, \tag{5}$$

$$\varepsilon Pe(U\theta_X + V\theta_Y) = \theta_{YY}. \tag{6}$$

The convective terms have to be taken into account since the Prandtl numbers of some liquids are relatively large. As an example, 25% ethyl-alcohol water solution has a Prandtl number of $Pr = 22.06$ under normal conditions.

Let us formulate the boundary conditions in non-dimensional forms. The initial temperature is assumed to be

$$\theta = 0. \tag{7}$$

At the bottom wall of the channel, $Y = 0$, there is a non-slip condition:

$$U = V = 0. \tag{8}$$

The presence of a local heater at the bottom is specified by a constant heat flux at the heating area. Denoting $\eta(X) = \chi(X) - \chi(X-1)$, we write this condition in a non-dimensional form as follows:

$$-\theta_Y = \varepsilon Pe\eta(X). \tag{9}$$

We formulate now the boundary condition at the liquid–gas interface, which is described by its non-dimensional thickness, $\bar{h}$. The kinematic condition is written as follows:

$$\bar{h}_X U = V. \tag{10}$$

Assume that the surface tension is a linear function of temperature,

$$\sigma = \sigma_0 - \sigma_T(T - T_0)$$

with $\sigma_0 > 0$, $\sigma_T > 0$ for typical liquids, then the interfacial stress conditions can be written as

$$P = -\overline{C}^{-1}\bar{h}_{XX}, \tag{11}$$

$$U_Y + Ma\bar{\theta}_X - \mathrm{T} = 0. \tag{12}$$

Ma is the Marangoni number defined as $Ma = \frac{\varepsilon\sigma_T\Delta T}{\mu\bar{u}}$, $\overline{C} = \frac{\bar{u}\mu}{\sigma_0}\varepsilon^{-3}$ is an analogue of capillary number, $\overline{C} = \mathrm{O}(1)$ as $\varepsilon \to 0$, which is applied for sufficiently strong surface-tension effects [29].

The boundary condition for temperature at the interface is Newton's cooling law, in which the heat flux normal to the interface is analogous to the temperature difference between the interface and the gas phase:

$$\theta_Y = -Bi(\theta - \theta_g), \tag{13}$$

where $Bi = \alpha h_0/\lambda$ is the Biot number. The temperature of gas phase θ_g is assumed constant in Section 3.

3.2. Temperature distribution

Consider the problem of heat transfer (6), (7), (9), and (13) for a rigid film ($h = h_0 = \mathrm{const}$) and a linear velocity profile $U = 2Y$ with $V = 0$. Using the method described in [32], we obtain the exact solution to the problem of temperature distribution:

$$\theta(X,Y)=\left(1+\frac{1}{Bi}-Y\right)\varepsilon Pe\eta(X)+\theta_g-\sum_{i=1}^{\infty}G_i\psi_i(Y)\exp(-\xi_i^2X)\frac{1}{\xi_i^2}\left[Bi\theta_g\psi_i(1)+\varepsilon Pe\psi_i(0)\left(\eta(0)+\int_0^X\exp(\xi_i^2X)\frac{\partial\eta(X)}{\partial X}\,dX\right)\right], \tag{14}$$

where $\psi_i(Y)=\sqrt{Y}J_{-1/3}\left(\frac{2}{3}\sqrt{2\varepsilon Pe}\xi_iY^{3/2}\right)$, $\xi_i(i=1,\ldots,\infty)$ are the eigenfunctions and eigenvalues of the Sturm–Liouville problem; $J_v(\xi)=\sum_{k=0}^{\infty}\frac{(-1)^k\left(\frac{\xi}{2}\right)^{v+2k}}{k!\overline{\Gamma}(v+k+1)}$ is the Bessel function of the first kind and $\overline{\Gamma}(k)$ is the gamma function. The coefficients G_i are determined from the condition of orthogonality of the eigenfunctions:

$$G_i=\frac{2\xi_i}{\left|\left(\frac{\partial\psi_i}{\partial\xi}(1)\right)_{\xi=\xi_i}\frac{\partial\psi_i}{\partial Y}(1)-\psi_i(1)\left(\frac{\partial^2\psi_i}{\partial Y\partial\xi}(1)\right)_{\xi=\xi_i}\right|}.$$

The series in sum (14) is rapidly convergent and summable. Note that solution (14) is valid for any function η possessing an integrable generalized derivative. In the case of $Bi\to 0$, the heat transfer problem (6), (7) and (9) should be considered with the thermal insulation boundary condition at the film surface $\theta_Y(X,\bar{h}(X))=0$ instead of (13).

The temperature distributions on the film surface of FC-72, calculated according to (14) for different liquid flow rates, are presented in Fig. 2. The position of the maximum of the temperature is replacing downstream with the increasing *Re* number. The influence of the convective heat transfer mechanism is much more prominent for relatively high values of the liquid Reynolds number. The thermal entry length also increases with increasing *Re*. The thermal entry length is defined as the average distance between the beginning of a heater and the point where the thermal boundary layer reaches the film surface. This point corresponds to the onset of the approximately linear rise of temperature (Fig. 2). The importance of both conductive and convective heat transfer in the liquid film is shown. The temperature reduction downstream of the heater is explained by heat transfer between the surface of the liquid film and the gas flow. The influence of the heat transfer between the film surface and the gas flow on temperature of the liquid is shown in Fig. 3. A variation of the Biot number in the range 0.005–1 corresponds to the variation of heat transfer coefficient on the film surface from 1.02 W/m^2 K to 203.1 W/m^2 K. As the Biot number increases, this corresponds to increasing of intensity of heat exchange with gas phase, the maximal film surface temperature decreases. The temperature reduction is more noticeable at smaller *Re* numbers (Fig. 2) and at greater *Bi* number (Fig. 3).

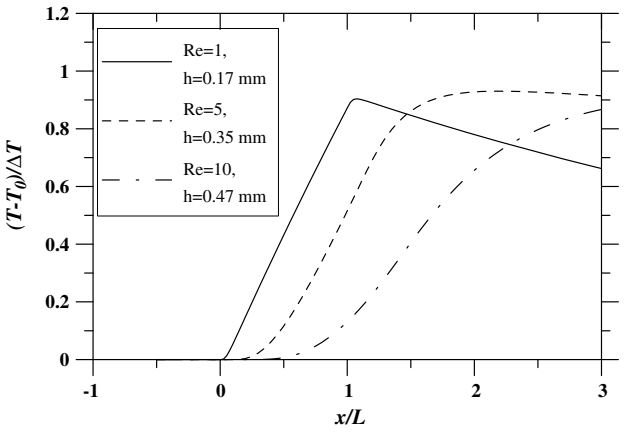

Fig. 2. The temperature distribution on the film surface, FC-72, $T_g=T_0=17$ °C, $L=6.7$ mm, $\varphi=0°$, $\alpha=20$ W/K m^2, $Re_g=242.8$, and the heater is situated from 0 to 1 along the *x*-axis.

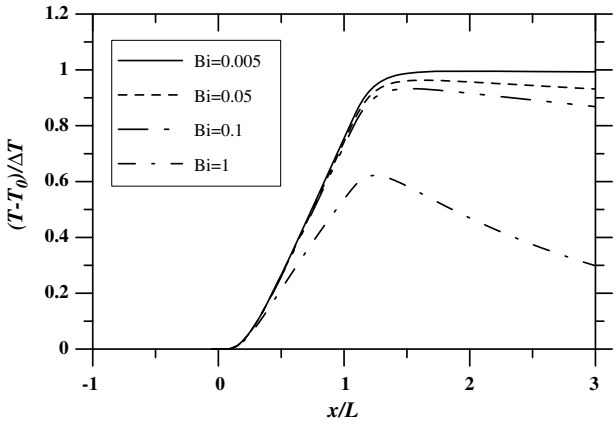

Fig. 3. The effect of Biot number on the temperature distribution on the film surface, FC-72, $T_g=T_0=30$ °C, $L=10$ mm, $\varphi=0°$, $Re=4.9$, $\tau=0.025$ kg/s^2 m.

3.3. Film deformation

The non-zero temperature gradient on the film surface leads to the thermocapillary so that the film is deformed by the Marangoni stresses. If the temperature distribution on the liquid surface is known, for instance from the analytical solution (14) or from experimental data, it is possible to find the values of the deformations.

The equation of continuity (5) and the kinematic condition (10) give the conservation of mass condition:

$$\frac{\partial}{\partial X}\int_0^{\bar{h}(X)}U(X,Y)dY=0. \tag{15}$$

The pressure from (4) with boundary condition (11) can be expressed as

$$P=-\overline{C}^{-1}\bar{h}_{XX}+\rho g h_0(\bar{h}-Y)\cos\varphi/\bar{p}.$$

Substituting this expression for pressure into Eq. (3) and integrating it twice gives the differential equation for the film thickness $\bar{h}(X)$:

$$\frac{\bar{h}^3}{3}\left(\varepsilon\overline{C}^{-1}\bar{h}_{XXX}-\varepsilon\frac{\rho g h_0}{\bar{p}}\cos\varphi\bar{h}_X+\frac{\rho g h_0}{\bar{p}}\sin\varphi\right)+\frac{\bar{h}^2}{2}\varepsilon(\mathrm{T}-Ma\bar{\theta}_X)=\varepsilon\gamma, \tag{16}$$

where γ is dimensionless flow rate.

Assume that $\bar{h}(X)=1+h_1(X)$, where $|h_1|\ll 1$. Linearizing Eq. (16) and neglecting the term $\varepsilon h_1 Ma\bar{\theta}_X=\mathrm{O}(\varepsilon^2)$ in the left-hand part (i.e., assuming that $Ma\ll 1$), we obtain the following linearized equation:

$$h_{1XXX}-\overline{C}\frac{\rho g h_0}{\bar{p}}\cos\varphi h_{1X}+3\overline{C}\left(\mathrm{T}+\frac{\rho g h_0}{\varepsilon\bar{p}}\sin\varphi\right)h_1=f(X), \tag{17}$$

where $f(X)=3\overline{C}(\gamma-\mathrm{T}/2+Ma\bar{\theta}_X/2)-\rho g h_0\overline{C}\sin\varphi/\varepsilon\bar{p}$. The thermocapillary force cannot be neglected in the right-hand section. This term $\varepsilon Ma\bar{\theta}_X/2=\mathrm{O}(\varepsilon)$ is of a lower order than $\mathrm{O}(\varepsilon^2)$. For a horizontal channel, $\gamma=1$, $\mathrm{T}=2$, and Eq. (17) simplifies to

$$h_{1XXX}-\overline{C}\frac{\rho g h_0}{\bar{p}}h_{1X}+3\overline{C}\mathrm{T}h_1=\frac{3}{2}\overline{C}Ma\bar{\theta}_X. \tag{18}$$

A solution to Eq. (17) is given by a convolution of the functions $F(X)$ and f [33]:

$$h_1(X)=\int_{-\infty}^{\infty}F(X-\xi)f(\xi)\mathrm{d}\xi. \tag{19}$$

Here, $F(X)$ is the fundamental solution of the corresponding homogeneous equation. The form of the fundamental solution depends on the sign of the discriminant of the characteristic polynomial:

$$s^3-\overline{C}\frac{\rho g h_0}{\bar{p}}\cos\varphi s+3\overline{C}\left(\mathrm{T}+\frac{\rho g h_0}{\varepsilon\bar{p}}\sin\varphi\right)=0. \tag{20}$$

The roots of the polynomial can be easily determined by Cardano's method. If the discriminant is positive, the latter polynomial has a single real root and two conjugated complex roots. Therefore, the fundamental solution to the left origin is a periodic function. In terms of the "zeroth discriminant", all roots are real and two coincide. For the negative discriminant, all roots are real and have different values. In the last two cases, the fundamental solution is not a periodic function. The details of the fundamental solution can be found in Appendix A.

Now, the case of the positive discriminant will be analysed in order to clarify the occurrence of possible perturbations. We have $-\left(\frac{\rho g}{3\sigma_0}\cos\varphi\right)^3+\left(\frac{3}{2\sigma_0 h_0}\left(\frac{\tau}{h_0}+\rho g\sin\varphi\right)\right)^2>0$. Denoting the capillary length as $l_\sigma=\sqrt{\frac{\sigma_0}{\rho g}}$, the condition of the positive discriminant is equivalent to the following inequality [16]:

$$\tau+\rho g h_0\sin\varphi>\rho g h_0\frac{2}{3}\frac{h_0}{l_\sigma}\left(\frac{\cos\varphi}{3}\right)^{3/2}. \tag{21}$$

Introducing an associated Bond number $Bo^*=\frac{\rho g h_0\cos\varphi}{\sigma_0/h_0}=Bo\cdot\cos\varphi$, which characterizes the ratio of gravitational forces to surface tension forces, condition (21) can be rewritten as

$$\tau+\rho g h_0\sin\varphi>\frac{2}{9\sqrt{3}}\sqrt{Bo^*}\rho g h_0\cos\varphi. \tag{22}$$

If the film driving forces (shear stress and gravity) overbalance the hydrostatic forces, damped perturbations or "ripples" of free surface will exist upstream of the bump. Perturbations always exist when the inclination angle of the channel is high ($\varphi\approx 90°$). A low Bo^* number indicates that surface tension forces is important, this is exemplified by the appreciable "capillary" perturbations showed in Fig. 4, where $Bo^*=7.58\times 10^{-4}$, $Re=0.04$, film thickness $h_0=24$ μm. Under conditions of microgravity, the damped perturbations of the free surface take place at any $\tau>0$ (Fig. 5b). The fundamental solution and expression for film thickness take the forms:

$$\begin{aligned}F(X)&=(\chi(X)\exp(-cX)+2\chi(-X)\exp(cX/2)\\&\quad\times\cos(\pi/3+\sqrt{3}cX/2))/3c^2,\\h_1(X)&=\int_{-\infty}^{\infty}F(X-\xi)3\overline{C}Ma\bar{\theta}_X/2\,\mathrm{d}\xi,\end{aligned} \tag{23}$$

where $c=(3\overline{C}\mathrm{T})^{1/3}$.

A trough of up to 5–10% of the initial film thickness was detected upstream of the bump for locally heated falling liquid films [31,34], which qualitatively validates the obtained result.

Fig. 5 and expressions (23) clearly demonstrate the thermocapillary character of film thinning in the vicinity of the lower edge of the heater. The calculated relative film thicknesses along the channel for different heat-transfer coefficients and for different tangential stresses are presented in Fig. 6 and 7. The positive temperature gradient in the heater area is the cause of the tangential stress induced by thermocapillary forces, and is directed against the main flow. Therefore, an increase in film thickness is observed in the heating area. Downstream from the heater, the temperature of the film surface decreases (Figs. 5–7) for comparatively small Reynolds numbers. The Marangoni force is directed streamwise in this area, causing a decrease in the film thickness. The minimum film thickness occurs under the maximal Biot number/heat-transfer coefficient, because for this case the absolute value of surface temperature gradient is maximal. This region is the riskiest one for a film

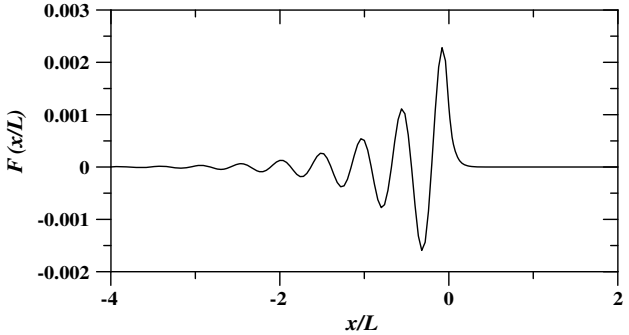

Fig. 4. Fundamental solution for FC-72, $T_0=17$ °C, $Re=0.04$, $\varphi=5°$, $\tau=0.024$ kg/s^2 m.

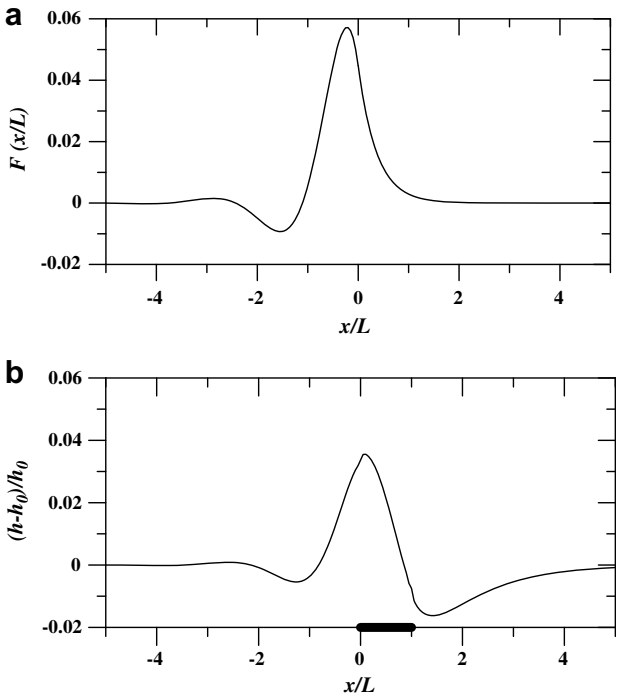

Fig. 5. $g = 0$, $D > 0$, H_2O, $T_g = T_0 = 17\ ^\circ C$, $L = 2$ mm, $Re = 1$, $q_0 = 0.1$ W/cm^2, $Bi = 0.29$, $h_0 = 76.3$ μm, $\tau = 0.363$ kg/s^2 m. a – fundamental solution, b – film deformation.

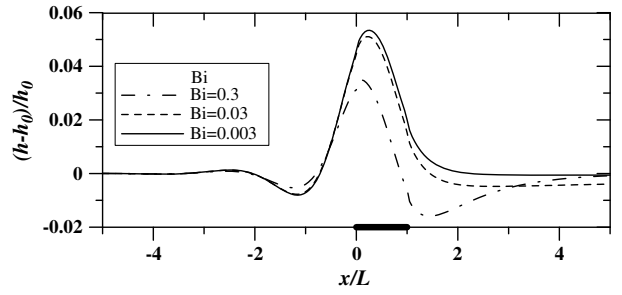

Fig. 6. Film thermocapillary deformation for different Biot numbers: H_2O, $g = 0$, $T_g = T_0 = 17\ ^\circ C$, $L = 2$ mm, $Re = 1$, $q_0 = 0.1$ W/cm^2, $h_0 = 76.3$ μm, $\tau = 0.363$ kg/s^2 m.

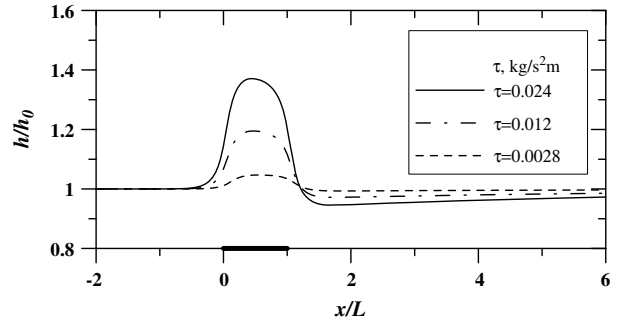

Fig. 7. Film thermocapillary deformation for different tangential stresses: FC-72, $T_g = T_0 = 17\ ^\circ C$, $L = 6.7$ mm, $Re = 1$, $q_0 = 0.1$ W/cm^2, $\varphi = 0^\circ$, $\alpha = 20$ W/m^2 K.

breakdown. A variation of $Bi = 0.003$; 0.03; 0.3 corresponds to $\alpha = 23.6$; 236; 2360 W/m^2 K, respectively. The position of the thermocapillary bump is determined by the thermal entry length.

The damped upstream perturbations of free surface are missing in Fig. 7 since condition (21) is not satisfied (i.e., the film driving force induced by gas flow is suppressed by hydrostatic forces). For a constant Re number, an increase in the tangential stress τ (corresponding to a growth of the gas flow rate) leads to a decrease of the initial film thickness, which enhances the thermocapillary effect. This calculation predicts thermocapillary thickening of up to 30–40% compared with the initial film thickness at low rates of heat transfer to the gas phase. A thermocapillary bump of analogous size to the order of magnitude has been observed in experiments for locally heated falling liquid film under gravity along a vertical plate [31,34].

The linear theory is applicable for relatively small values of the Marangoni number (i.e., for relatively small heat fluxes). It was shown in [11] that for heat flux densities under 2 W/cm^2, linear theories agreed with the experimental data and with direct numerical simulation of film thickness for gravity-driven liquid films.

4. Evaporation effect

4.1. Formulation

The problem described in Section 3 does not account for the effect of evaporation. The heat transfer to gas has been approximated using a constant Biot number. However, heating and evaporation of the liquid produce heat and mass transfers at the liquid–gas interface. Since a heated shear-driven liquid film with relatively small initial thickness (~100 μm) is examined, which is subjected to heat fluxes up to 10–50 W/cm^2, the process of evaporation will play a significant role and must be considered. On the other hand, one of the peculiarities of the modelling problem is local heating. This brings up the question: How do evaporation processes influence global heat transfer and its enhancement? In order to answer this question, the heat and mass transfer problem for shear-driven films is considered in this section. We do not concern ourselves with the problem of film deformation due to evaporation and thermocapillarity; nevertheless, some comments on film deformation will be provided at the end of the section.

It is assumed that the gas velocity is 2–3 orders of magnitude greater than the liquid velocity, and that the operating regime is laminar in both the gas and liquid phases. Experimental investigations of isothermal shear-driven liquid films justify that for small liquid and gas flow rates, the film surface is smooth throughout the length of the channel. Furthermore, an initial section of smooth film always exists [30]. Accordingly, this theoretical investigation is considered in the framework of such flow regimes with velocity profiles for laminar co-current parallel streams (1), (2) and with non-deformable film surfaces

(Section 2). It is reasonable to assume that the total mass flow rate of evaporated liquid is much lower than the total mass flow rate of liquid film. Also, evaporated substance is a small impurity in gas, which scarcely affects gas thermodynamic properties. These last two assumptions may cause a limitation on the intensity of heating.

Calculations are carried out for water (with relatively high latent heat) and air (with a relative humidity of 0.2), similarly to the working liquid and gas, which have been used in experiments. The gas is considered to be ideal and incompressible. The physicochemical and transport properties of the gas phase are considered to be uniform, and are computed for fixed temperature, pressure and given relative humidity by means of mixing rules [35] applicable to any multi-component mixture (see Appendix B). The physicochemical and transport properties of the liquid film are taken at the fixed initial temperature.

We consider here the 2D heat and mass transfer problem for rigid liquid film and gas flow in a microchannel with a local heater. The convective terms in the energy equations and convection–diffusion equation are taken into account:

$$u\frac{\partial T}{\partial x} = a\frac{\partial^2 T}{\partial y^2}, \tag{24}$$

$$u_g\frac{\partial T_g}{\partial x} = a_g\frac{\partial^2 T_g}{\partial y^2} + \frac{\mu_g}{\rho_g c_p^g}\left(\frac{\partial u_g}{\partial y}\right)^2, \tag{25}$$

$$u_g\frac{\partial C}{\partial x} = D\frac{\partial^2 C}{\partial y^2}. \tag{26}$$

The enthalpy diffusion term is negligible in the energy equation for the gas phase [23]. The impact of viscous dissipation on film temperature has been estimated and turned out to be insignificant, except for some temperature discrepancy observed in the gas phase (see Fig. 8). This is due to the fact that drops in temperature during the gas phase are small in comparison with temperature drops in liquid films. The results presented below take into consideration the dissipative term in equation (25). It should be noted that in microchannels, the effects of viscous dissipation can be important even under laminar flow [36].

Let us now formulate the boundary conditions. A constant initial temperature is given

$$\lim_{x\to-\infty} T(x,y) = \lim_{x\to-\infty} T_g(x,y) = T_0. \tag{27}$$

At the bottom wall, local heating is specified by the constant heat flux at the heater area:

$$-\lambda\left.\frac{\partial T}{\partial y}\right|_{y=0} = q_0(\chi(x) - \chi(x-L)). \tag{28}$$

The energy balance at the gas–liquid interface is described by

$$-\lambda\left.\frac{\partial T}{\partial y}\right|_{y=h} + \lambda_g\left.\frac{\partial T_g}{\partial y}\right|_{y=h} = -r\frac{1}{1-C^*/\rho_g}D\left.\frac{\partial C}{\partial y}\right|_{y=h}, \tag{29}$$

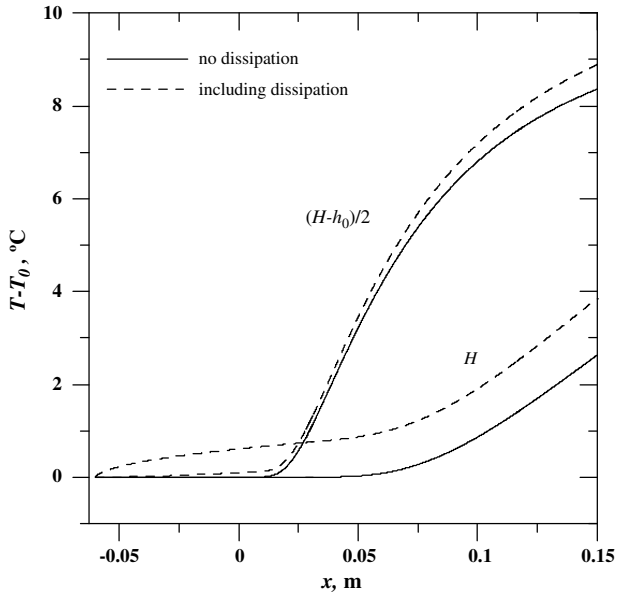

Fig. 8. Effect of viscous dissipation on gas temperature. $T_0 = 21$ °C, $q_0 = 10$ W/cm^2, $\varphi = 0°$, $H = 1$ mm, $L = 10$ mm, $Re = 1$, $Re_g = 2000$, $\Gamma_e/\Gamma = 0.043$.

where the mass flux $J = -\frac{1}{1-C^*/\rho_g}D\left.\frac{\partial C}{\partial y}\right|_{y=h}$ exchanged at the interface is given by applying Fick's law and supposing that the interface is impermeable to dry gas.

$$C|_{y=h} = C^*(T). \tag{30}$$

Eq. (30) is the equilibrium condition and has the following meaning. It is known that temperature and gas pressure variations influence the vapor concentration at the gas–liquid interface. The problem formulation assumes gas pressure variation to be insignificant. Therefore, its effect on water vapor concentration variation is negligible, so Henry's law is valid. An equilibrium concentration at the surface of the evaporating liquid is supposed to be linearly dependent on surface temperature $C^*(T) = C_0 + C_1(T(x,h) - T_0)$. For given temperatures T_0 and T_1, using the relative humidity of air, and gas total pressure, which is equal to normal pressure, we can find water vapor concentrations with the ideal gas law using saturated vapor partial pressure tabulations. Finally, we determine coefficients C_0 and C_1 by considering linear approximations of the equilibrium concentration on temperature:

$$C_0 = \frac{p_0 M_v}{RT_0}, \quad C_1 = \left(\frac{p_1 M_v}{RT_1} - C_0\right)\Big/(T_1 - T_0).$$

Thus, three simplifications have been made to obtain boundary condition (30) out of the equilibrium state equation: (1) equilibrium concentration depends on temperature only; (2) the ideal gas law is valid; (3) vapor concentration at the gas–liquid interface depends linearly on temperature. The latter assumption is considered for simplicity; generally, a polynomial dependence can be considered.

As an example, for a relative air humidity of 0.2, an initial temperature of $T_0 = 21$ °C and a possible temperature

deviation $T_1 - T_0 = 30$ °C, these coefficients have values $C_0 = 3.66 \times 10^{-3}$ kg/m^3 and $C_1 = 4.55 \times 10^{-4}$ kg/m^3 K for the water–humid air system. These values are used in most of the calculations presented below.

The upper wall $y = H$ is considered adiabatic:

$$\left.\frac{\partial T_g}{\partial y}\right|_{y=H} = 0 \tag{31}$$

and no mass flux is assumed on the upper wall:

$$\left.\frac{\partial C}{\partial y}\right|_{y=H} = 0. \tag{32}$$

Eqs. (24)–(32) are changed to dimensionless forms and approximated by difference schemes. Two systems of equations are obtained with tridiagonal matrices connected by boundary conditions, which can be efficiently solved iteratively by the sweep method. The numerical code is verified by the variation of mesh points and is tested by comparison with analytical solutions (Section 3). It is also in excellent agreement with experimental and numerical data for a gravity-driven liquid film of 25% ethyl alcohol in water with a thermal insulation boundary condition on the gas–liquid interface [11].

As long as the model implies that the film surface is non-deformable, it is necessary to verify a mass flow rate value of evaporated vapor, which is calculated as

$$\Gamma_e(x) = \int_{h_0}^{H} u_g(y) C(x,y) \mathrm{d}y.$$

It is reasonable to determine Γ_e at the end of the channel. This value depends on different flow parameters, such as the film and gas Reynolds numbers, heat flux, heater size, and channel height. We expect the model to be valid for $\Gamma_e/\Gamma \leqslant 0.2$.

4.2. Transport phenomena

To illustrate the effects of liquid Reynolds numbers on the bottom wall and interfacial temperatures, Fig. 9 presents the axial distributions of T_W and T_I, where flow regimes with Re equal to 3 and 10 correspond to film thicknesses of 76.6 μm and 127.7 μm, respectively. The influence of convective heat transfer in the liquid film is becoming noticeable with increasing *Re*, which results in an increase of the thermal entry length. The enhancement of gas velocity decreases the value of film thickness and increases liquid velocity, resulting in a reduction of wall and interfacial temperatures. The latter is explained by convective heat exchange between the liquid and gas streams and evaporation (Fig. 10). A similar situation takes place with decreasing the channel height.

Now, we analyze the enhancement of heat transfer from a local heat source. Fig. 11 demonstrates the contribution of different heat transfer mechanisms in the cooling of the local heater. Calculations are performed for three cases: 1 – only convection to the liquid film exists; 2 – convection

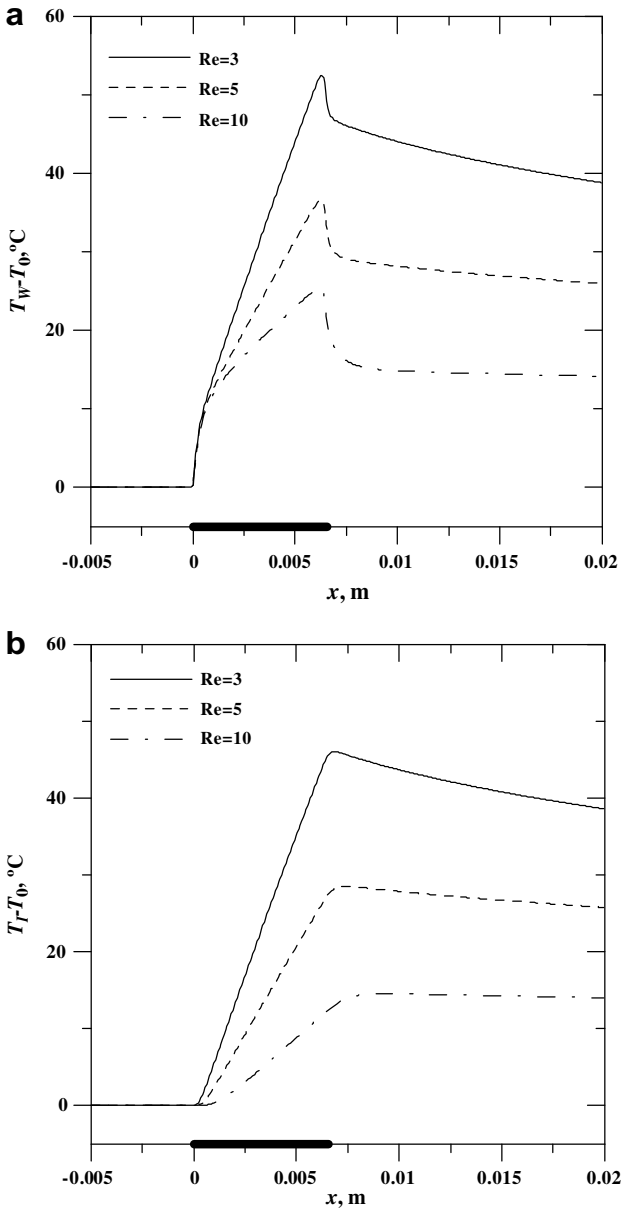

Fig. 9. Temperature distributions: a – on the bottom wall, b – on the gas–liquid interface. $T_0 = 21$ °C, $q_0 = 10$ W/cm^2, $\varphi = 0°$, $H = 1$ mm, $L = 6.55$ mm, $Re_g = 600$.

to the liquid and gas phases takes place; 3 – evaporation and convection to the liquid and gas takes place. The presence of evaporation decreases the heater temperature by 25.4 °C under these particular conditions. All three transport phenomena are important for relatively thin films, and the thermal entry length is a determining factor for heaters with finite length. Intensive evaporation starts when the thermal boundary layer reaches the film surface. Our calculations reveal that the thinner the film, the shorter the thermal entry length. The latter is proportional to $PrRe^{4/3}$, at least for gravity-driven films [37,38]. Also, the evaporation rate depends on heater length. This is illustrated in Fig. 12, where the thermal entry length is long

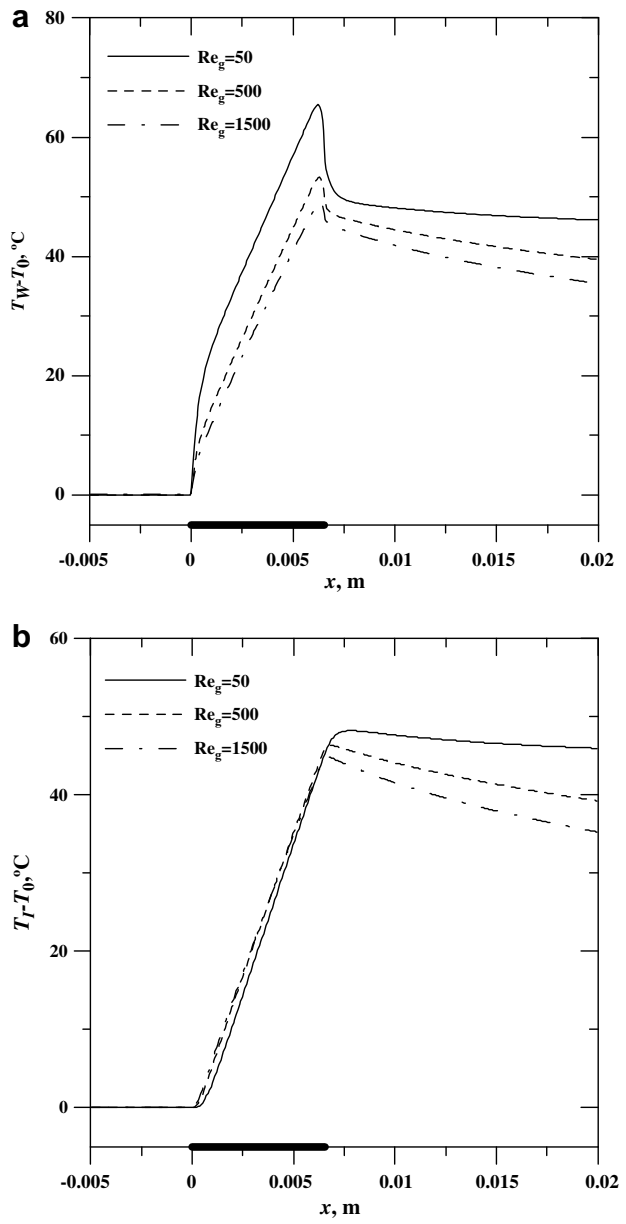

Fig. 10. Effect of gas Reynolds number: a – on the bottom wall, b – on gas–liquid interface temperature distributions. $T_0 = 21$ °C, $q_0 = 10$ W/cm^2, $\varphi = 0°$, $H = 1$ mm, $L = 6.55$ mm, $Re = 3$.

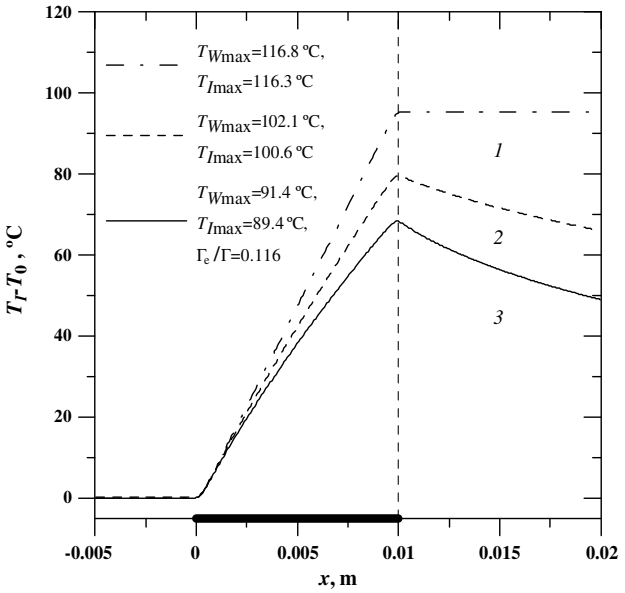

Fig. 11. Temperature distribution at the H_2O–air interface. Liquid film, gas flow and evaporation contributions to heat removal from the local heater. $\varphi = 0°$, $q_0 = 6$ W/cm^2, $Re = 1.5$, $H = 1$ mm, $L = 10$ mm, $Re_g = 1500$, $h_0 = 36.7$ μm.

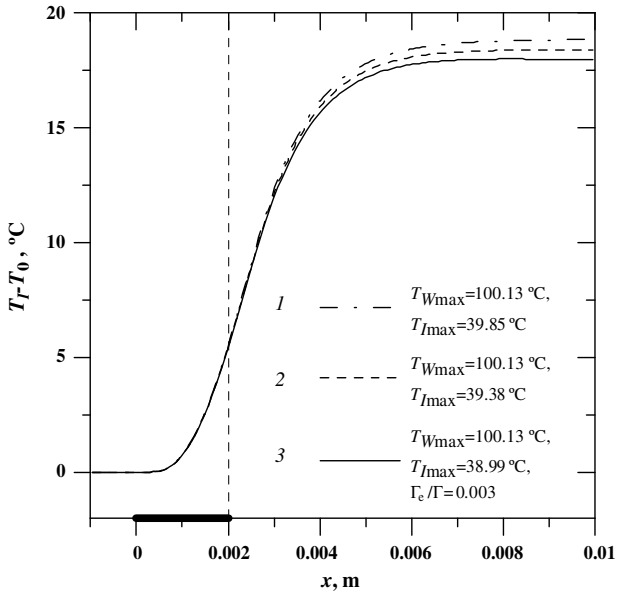

Fig. 12. Temperature distribution at the H_2O–air interface. The thermal boundary layer does not reach the film surface on the heating area. $\varphi = 0°$, $q_0 = 40$ W/cm^2, $Re = 10$, $H = 1$ mm, $L = 2$ mm, $Re_g = 200$, $h_0 = 194.8$ μm.

enough, with the result that the heater is mainly cooled by convection to the liquid film.

We have estimated the heat flux limit for the water–nitrogen system and for chosen wall temperature of $T_{Wmax} = 80$ °C depending on initial film thickness h_0 and heater length L. With reference to Fig. 10a, in Fig. 13 it can be seen that for flow regimes with $\Gamma_e/\Gamma < 0.1$, the threshold heat flux increases with an increase in both liquid and gas Reynolds numbers. The film thickness within 40–60 μm appears to be a critical region where the evaporation process markedly affects the film dynamics. Of course, not only film deformations, but also the change in liquid properties such as viscosity, heat of vaporization, etc., are important for heat transfer enhancement. Therefore, our subsequent works will be devoted to investigation of shear-driven liquid films with low latent heat of vaporization.

4.3. Biot number

Usually, a constant Biot number is used to study the instability problems of heated liquid films [12–15]. In order

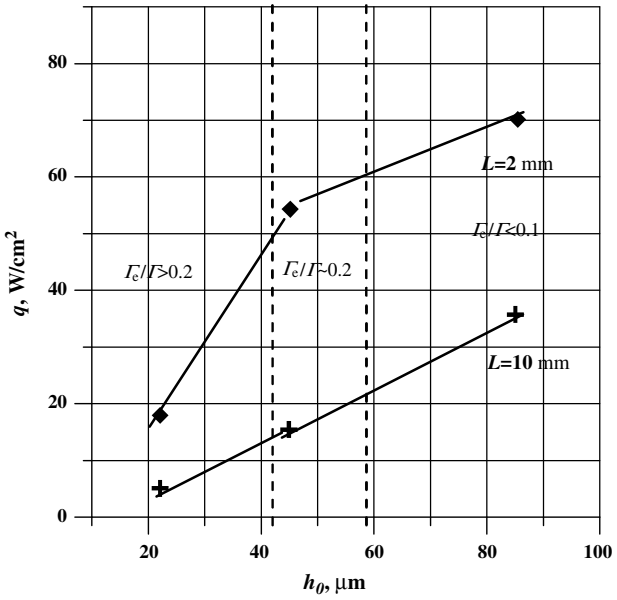

Fig. 13. Estimation of the heat flux limit for wall temperature $T_{Wmax} = 80$ °C depending on the initial film thickness h_0 and heater length L. Nitrogen $Re_g = 3000$, $H = 1$ mm, water $Re = 1$–20.

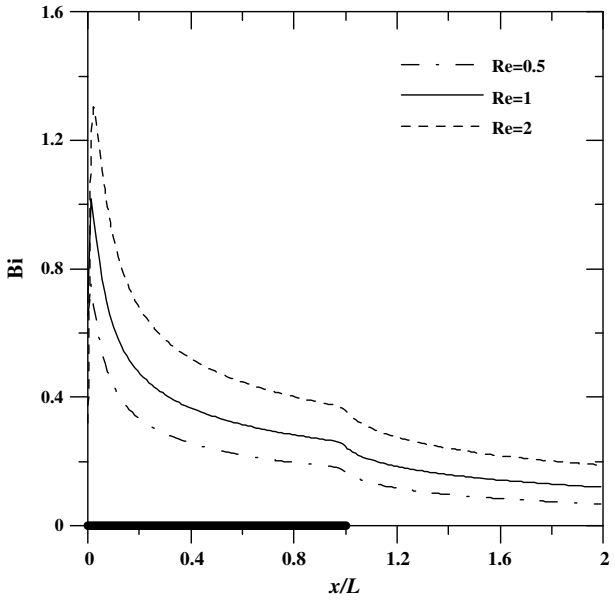

Fig. 14. Biot numbers at the H_2O–air phase interface. $T_0 = 21$ °C, $q_0 = 10$ W/cm^2, $\varphi = 0°$, $H = 1$ mm, $L = 6.55$ mm, $Re_g = 600$.

to improve the understanding of the interfacial heat transfer, we calculate the heat transfer coefficient at the gas–liquid interface using Newton's cooling law:

$$\alpha(x) = -\lambda \frac{\frac{\partial T}{\partial n}(x,h)}{T(x,h) - T_0}.$$

The Biot number as a function of parameters of the flow and spatial variable is found as

$$Bi(x) = \alpha(x)h/\lambda = -\frac{\frac{\partial T}{\partial n}(x,h)}{T(x,h) - T_0}h.$$

Fig. 14 and 15 demonstrate the behaviour of the Biot number and heat transfer coefficient versus spatial variables and liquid and gas Reynolds numbers, respectively. The dependence of the Biot number and heat transfer coefficient on the longitudinal axis has a sectional-hyperbolic character. The break of the curves in the vicinity of the lower edge of the heater is caused by the start of the temperature reduction. Such a variable Biot number can be substituted to Newton's cooling law (13) in order to define a film deformation in the lubrication-type approach.

In the heater region for $Re = 0.5$, a variation of Biot number in the range from 0.75 to 0.16 takes place that corresponds to a variation of the value of heat transfer coefficient on the film surface from 13563 W/m^2 K to 3018 W/m^2 K. For $Re = 1$, the variations of Bi and α are from 1.01 to 0.24 and from 13206 W/m^2 K to 3125 W/m^2 K, respectively. For $Re = 2$, these variations are from 1.30 to 0.35 and from 12319 W/m^2 K to 3330 W/m^2 K.

Note that the constant average Biot number for analytical solution (14) approximating the temperature distribution in a heater area can be found minimizing the difference between film surface temperatures, $\min_{0 \leqslant x \leqslant L} |T_I^*(x,h) - T_I(x,h)|$. Here, $T_I^*(x,h)$ and $T_I(x,h)$ are gas–liquid interface temperatures corresponding to an exact solution (14) and to a numerical solution of (24)–(32), respectively. Though the average value from the beginning of the heater to the point of stabilization of the heat transfer coefficient gives a rather good agreement between temperatures $T_I^*(x,h)$ and $T_I(x,h)$ in the heater area, outside of the heater, the temperature $T_I^*(x,h)$ reduces drastically. This is associated with overestimation of the value Biot number downstream from the heater.

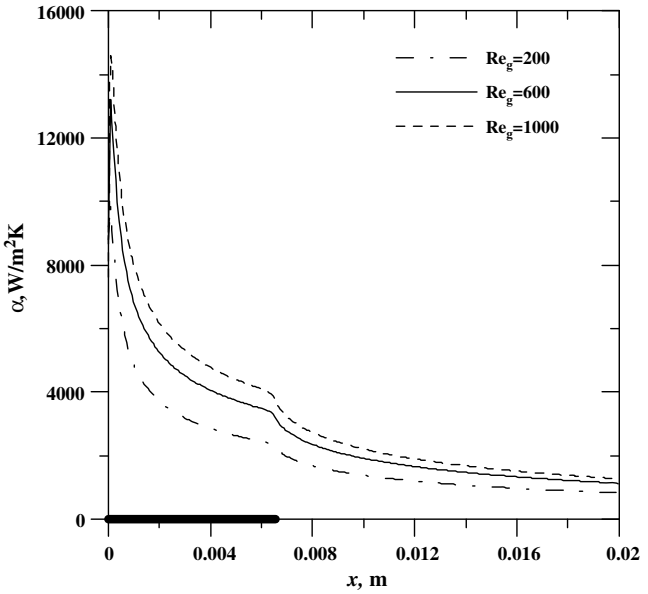

Fig. 15. The heat transfer coefficient at the H_2O–air phase interface. $T_0 = 21$ °C, $q_0 = 10$ W/cm^2, $\varphi = 0°$, $H = 1$ mm, $L = 6.55$ mm, $Re = 1$.

4.4. Comparison with experimental data

Available experimental investigations with local heating of a liquid film are described in [30]. The test section was set horizontally, and the heater of 22×6.55 mm size was embedded into a thermostabilizing copper block.

Water and air with a relative humidity of ~0.2 were used as the working liquid and gas, respectively. Experiments were carried out at atmospheric pressure. The initial temperature of the gas was equal to ambient temperature, or 22–25 °C, and the channel height was 2 mm.

Temperature distributions at the film surface measured by an infrared scanner are compared with numerical data (Fig. 16). Heat flux has a noticeable effect on streamwise temperature distribution at the film surface. The main difficulty is that the temperature (heat flux) distribution at the experimental heater wall is unknown. This distribution depends on many factors, such as the shape and size of the heater, the properties of the heater and channel materials, liquid properties, etc. The most consistent approach would be to solve a fully coupled problem including the thermal conduction in the heater. Keeping in mind that there are temperature stabilizers outside of the heater, we choose the boundary condition on the bottom wall for calculations as follows:

$$\begin{cases} \lambda \frac{\partial T}{\partial y}\Big|_{y=0} = -q(x), \quad x_0 \leqslant x \leqslant x_0 + L, \\ T(x,0) = T_0, \quad \text{otherwise}, \end{cases}$$

$$\text{where } q(x) = \begin{cases} q_0 - \left|\frac{x - L/2}{L/2}\right|^n, & 0 \leqslant x \leqslant x_m, \\ q_0 - \left|\frac{x - x_m}{L - x_m}\right|^2, & x_m < x \leqslant L. \end{cases}$$

The heat flux distribution incorporates a fall in flux value due to the heating of the liquid film, which qualitatively corresponds to numerical simulations of heat flux distribution for locally heated gravity-driven films [38]. In the simulations, we assume $x_m = L/3$, $n = 26$.

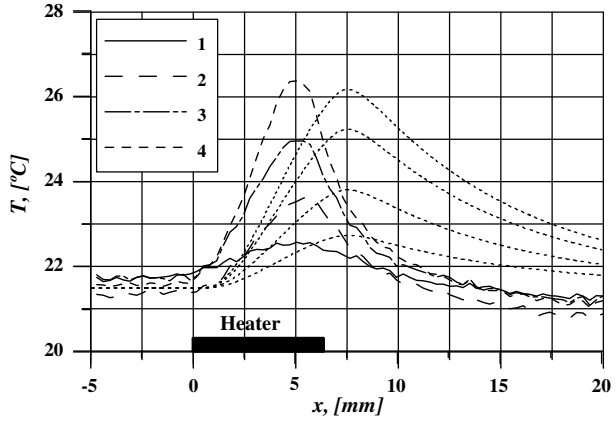

Fig. 16. Temperature at the film surface averaged over the heater width, $Re = 8.5$, $Re_g = 534$, 1 – $q_0 = 1.01$ W/cm^2, 2 – 1.88 W/cm^2, 3 – 3.04 W/cm^2, 4 – 3.8 W/cm^2. Thick lines – experimental data, thin dotted lines – calculated data.

Calculations satisfactorily describe the maximal surface temperature values, T_{Imax}, difference forms ~0.3 °C (Fig. 16), and predict maximal water–air interface temperature position at the bottom edge of the heater. Such a T_{Imax} position has been shown in experiments and numerical investigations of gravitationally falling liquid films [11]. In the experimental data [30], the maximum surface temperature is located upstream of the bottom edge of the heater. Most probably, this discrepancy can be due to the boundary condition disagreement. In view of the fact that the measured film surface temperature in crosswise direction of heater is quit non-uniform even for low heat fluxes and for smooth film [30]. Unfortunately, we cannot give any information about the real experimental condition in the heater. Nevertheless, the fact of the temperatures discrepancy may be attributed to the 3D deformation and thinning of liquid films [16,30] due to Marangoni forces at the end of heater, along with the intensive evaporation in this area [39]. This non-uniform evaporation effect may result in thermal Marangoni flow. More detailed experiments with greater measurement accuracy are needed to verify the experimental results in Fig. 16 and to validate the proposed theoretical model.

5. Conclusions

In this study we consider the problem of locally heated liquid film flow sheared by gas flow in a mini/microchannel. Heat transfer and thermocapillary film deformation problems for weakly heated liquid films have been treated in the framework of a one-sided 2D model. The exact solution for the heat transfer problem obtained for a linear velocity profile shows that the influence of a convective heat transfer mechanism is much more prominent for relatively high values of liquid Reynolds number, starting with estimating value of film Reynolds number $Re = 4.5$. Thermocapillary forces are shown to lead to the film thinning in the vicinity of the heater's lower edge and to the formation of a liquid bump in the vicinity of the upper edge, and additional damped perturbations of the free surface may occur upstream of the bump. A criterion is found that indicates that these "ripples" always exist under microgravity conditions or for vertically situated channels, which is in qualitative agreement with the experimental results.

The problem of heat and mass transfer has been examined in the framework of a two-sided 2D model. The model includes the energy equations for liquid and gas phases, and the convection–diffusion equation with the appropriate boundary conditions. All the equations consider the Peclet numbers O(1) or larger and include the convective terms and expected to be valid for laminar flows in both the liquid and gas phases (for moderate Reynolds numbers). The evaporation effect on heat transfer has been analyzed numerically, and it is shown that evaporation dramatically changes the temperature distribution, and hence, thermocapillary forces on the gas–liquid interface, even when

the mass flow rate of the evaporated liquid is much lower than the mass flow rate of the liquid film. The thermal boundary layer has been found to play an important role in evaporation intensity, resulting in the cooling of the local heater by shear-driven liquid film. The thermal entry length increases with increasing film thickness. Film thickness and the emergence of the thermal boundary layer can be regulated by gas flow rate/velocity or channel height. The temperature distribution at the film surface measured by an infrared scanner has been compared with numerical data, and the maximal surface temperature values are in good agreement.

The dependence of the Biot number on flow parameters and spatial variables was obtained numerically. The Biot number, as a function of the longitudinal axis, has a sectional-hyperbolic character. Hence, we have showed that approximation by constant Biot number can be a source of high uncertainty when studying the non-linear dynamics of locally heated liquid films.

On the whole, the heat transfer from liquid to gas flow and evaporation enhance the heat removal from the local heater, making shear-driven liquid films more suitable for cooling applications than gravity-driven films. According to the numerical results, all heat transfer mechanisms – convections to the liquid and gas phases as well as evaporation – are important for a global cooling effect.

Acknowledgements

The authors gratefully acknowledge support of this work by RFBR (No. 05-08-65426) and CRDF (No. RUE1-2846-NO-06). E.G. acknowledges the hospitality of the Microgravity Research Center at ULB, as well as support from INTAS, Grant No. 05-109-5022 and from a Grant by the President of the Russian Federation No. MK-2964.2007.8. We thank V. Ajaev who has read the manuscript and made valuable suggestions.

Appendix A

$s_1 = -c, s_{1,2} = \frac{c}{2} \pm \mathrm{i}b$ are the roots of the characteristic polynomial (20), where

$$c = \sqrt[3]{\frac{3}{2}\overline{C}\left(\mathrm{T} + \frac{\rho g h_0}{\varepsilon \bar{p}} \sin\varphi\right) - \sqrt{\Omega}} + \sqrt[3]{\frac{3}{2}\overline{C}\left(\mathrm{T} + \frac{\rho g h_0}{\varepsilon \bar{p}} \sin\varphi\right) + \sqrt{\Omega}}$$

$$b = \frac{\sqrt{3}}{2}\left(\sqrt[3]{-\frac{3}{2}\overline{C}\left(\mathrm{T} + \frac{\rho g h_0}{\varepsilon \bar{p}} \sin\varphi\right) + \sqrt{\Omega}} - \sqrt[3]{-\frac{3}{2}\overline{C}\left(\mathrm{T} + \frac{\rho g h_0}{\varepsilon \bar{p}} \sin\varphi\right) - \sqrt{\Omega}}\right)$$

$\Omega = -\left(\frac{\rho g h_0 \overline{C}}{3\bar{p}} \cos\varphi\right)^3 + \left(\frac{3}{2}\overline{C}\left(\mathrm{T} + \frac{\rho g h_0}{\varepsilon \bar{p}} \sin\varphi\right)\right)^2$ is the discriminant of polynomial (20).

The fundamental solution has the following forms:

$$F(X) = \frac{4}{9c^2 + 4b^2}\left(\chi(X)\exp(-cX) + \chi(-X)\exp\left(\frac{c}{2}X\right) \times \left(\cos(bX) - \frac{3c}{2b}\sin(bX)\right)\right), \quad \text{when } \Omega > 0;$$

$$F(X) = \frac{4}{9c^2}\left(\chi(X)\exp(-cX) + \chi(-X)\exp\left(\frac{c}{2}X\right) \times \left(1 - \frac{3c}{2}X\right)\right), \quad \text{when } \Omega = 0;$$

$$F(X) = \frac{\chi(-X\,\mathrm{sgn}s_1)\exp(s_1X)}{(s_1 - s_2)(s_1 - s_3)} + \frac{\chi(-X\,\mathrm{sgn}s_2)\exp(s_2X)}{(s_2 - s_1)(s_2 - s_3)} + \frac{\chi(-X\,\mathrm{sgn}s_3)\exp(s_3X)}{(s_3 - s_1)(s_3 - s_2)}, \quad \text{when } \Omega < 0.$$

Appendix B

$$\rho_\mathrm{g} = \frac{M_\mathrm{g} p_\mathrm{g}}{RT_0}\ \mathrm{kg/m^3}, \quad m_\mathrm{v} = 0.2, \quad m_\mathrm{a} = 1 - m_\mathrm{v} = 0.8$$

$$M_\mathrm{g} = \frac{1}{m_\mathrm{v}/M_\mathrm{v} + m_\mathrm{a}/M_\mathrm{a}}\ \mathrm{kg/mol}, \quad M_\mathrm{v} = 18 \times 10^{-3}\ \mathrm{kg/mol},$$

$$M_\mathrm{a} = 29 \times 10^{-3}\ \mathrm{kg/mol}$$

$$c_p^\mathrm{g} = m_\mathrm{v}c_p^\mathrm{v} + m_\mathrm{a}c_p^\mathrm{a} = 4185[0.24m_\mathrm{a} + 0.46m_\mathrm{v}]\ \mathrm{J/kg\ K}$$

$$D = 2.05 \times 10^{-5}\left(\frac{T_0}{273}\right)^{2.072}\ \mathrm{m^2/s}$$

$$r = 4185(597 - 0.56(T_0 - 273))\ \mathrm{J/kg}$$

$$\lambda_\mathrm{g} = \lambda_\mathrm{a} + 4.76 \times 10^{-3}\frac{m_\mathrm{v}}{m_\mathrm{a}}\ \mathrm{W/m\ K}$$

$$\mu_\mathrm{g} = \frac{\mu_\mathrm{v}X_\mathrm{v}}{X_\mathrm{v} + X_\mathrm{a}\alpha_{\mathrm{v,a}}} + \frac{\mu_\mathrm{a}X_\mathrm{a}}{X_\mathrm{a} + X_\mathrm{v}\alpha_{\mathrm{a,v}}}\ \mathrm{kg/m\ s},$$

where $X_\mathrm{a} = m_\mathrm{a}\frac{M_\mathrm{g}}{M_\mathrm{a}}, \quad X_\mathrm{v} = m_\mathrm{v}\frac{M_\mathrm{g}}{M_\mathrm{v}},$

$$\alpha_{\mathrm{v,a}} = \frac{\left(1 + \sqrt{\mu_\mathrm{v}/\mu_\mathrm{a}}\sqrt[4]{M_\mathrm{a}/M_\mathrm{v}}\right)^2}{\sqrt{8}\sqrt{1 + M_\mathrm{v}/M_\mathrm{a}}},$$

$$\alpha_{\mathrm{a,v}} = \frac{\left(1 + \sqrt{\mu_\mathrm{a}/\mu_\mathrm{v}}\sqrt[4]{M_\mathrm{v}/M_\mathrm{a}}\right)^2}{\sqrt{8}\sqrt{1 + M_\mathrm{a}/M_\mathrm{v}}}.$$

References

[1] T.J. Hanratty, J.M. Engen, Interaction between a turbulent air stream and moving water surface, AIChE J. 3 (1957) 299–304.
[2] G.F. Hewitt, M.S. Hall-Taylor, Annular Two-Phase Flow, Pergamon Press, Oxford, 1970.
[3] A.M. Cazabat, F. Heslot, S.M. Troian, P. Carles, Fingering instability of thin spreading films driven by temperature gradients, Nature 346 (1990) 824–826.
[4] O.A. Kabov, Formation of regular structures in a falling liquid film upon local heating, Thermophys. Aeromech. 5 (1) (1998) 547–551.

[5] M. Potash Jr., P.C. Wayner Jr., Evaporation from a two-dimensional extended meniscus, Int. J. Heat Mass Transfer 15 (1972) 1851–1863.
[6] M. Elbaum, S.G. Lipson, How does a thin wetted film dry up? Phys. Rev. Lett. 72 (22) (1994) 3562–3565.
[7] A. Bar-Cohen, G. Sherwood, M. Hodes, G.L. Solbreken, Gas-assisted evaporative cooling of high density electronic modules, IEEE Trans. CPMT Part A 18 (3) (1995) 502–509.
[8] O.A. Kabov, V.V. Kuznetsov, J.C. Legros, Heat transfer and film dynamic in shear-driven liquid film cooling system of microelectronic equipment, in: Proceedings of the Second International Conference on Microchannels and Minichannels, ASME, Rochester, 2004, pp. 687–694.
[9] R. Mahajan, C. Chiu, G. Chrysler, Cooling a microprocessor chip, Proc. IEEE 94 (8) (2006) 1476–1486.
[10] P. Stephan, C.A. Busse, Analysis of heat transfer coefficient of grooved heat pipe evaporator walls, Int. J. Heat Mass Transfer 35 (1992) 383–391.
[11] I.V. Marchuk, O.A. Kabov, Numerical modeling of thermocapillary reverse flow in thin liquid films under local heating, Russian J. Eng. Thermophys. 8 (1–4) (1998) 17–46.
[12] J.M. Skotheim, U. Thiele, B. Scheid, On the instability of a falling film due to localized heating, J. Fluid Mech. 475 (2003) 1–19.
[13] S. Kalliadasis, A. Kiyashko, E.A. Demekhin, Marangoni instability of a thin liquid film heated from below by a local heat source, J. Fluid Mech. 475 (2003) 377–408.
[14] A.M. Frank, 3D numerical simulation of regular structure formation in a locally heated falling film, Eur. J. Mech. B/Fluids 22 (2003) 445–471.
[15] A.M. Frank, O.A. Kabov, Thermocapillary structure formation in a falling film: experiment and calculations, Phys. Fluids 18 (2006) 032107.
[16] E.Ya. Gatapova, O.A. Kabov, I.V. Marchuk, Thermocapillary deformation of a locally heated liquid film moving under the action of a gas flow, Tech. Phys. Lett. 30 (5) (2004) 418–421.
[17] E.Ya. Gatapova, I.V. Marchuk, O.A. Kabov, Heat transfer and two-dimensional deformations in locally heated liquid film with co-current gas flow, J. Therm. Sci. Eng., Heat Transfer Soc. Jpn. 12 (1) (2004) 27–34.
[18] J.P. Burelbach, S.G. Bankoff, S.H. Davis, Nonlinear stability of evaporating/condensing liquid films, J. Fluid Mech. 195 (1988) 463–494.
[19] B. Haut, P. Colinet, Surface-tension-driven instabilities of a pure liquid layer evaporating into an inert gas, J. Colloid Interface Sci. 285 (1) (2005) 296–305.
[20] A.E. Hosoi, W.M. Bush, Evaporative instabilities in climbing films, J. Fluid Mech. 442 (2001) 217–239.
[21] H. Rosskamp, M. Willmann, S. Witting, Heat up and evaporation of shear driven liquid wall films in hot turbulent air flow, Int. J. Heat Fluid Flow 19 (1998) 167–172.
[22] W.-M. Yan, C.-Y. Soong, Convective heat and mass transfer along an inclined heated plate with film evaporation, Int. J. Heat Mass Transfer 38 (7) (1995) 1261–1269.
[23] E.H. Mezaache, M. Daguenet, Etude numerique de l'evaporation dans un courant d'air humide laminaire d'un film d'eau ruisselant sur une plaque incline, Int. J. Therm. Sci. 39 (2000) 117–129.
[24] S. Ben Jabrallah, A. Belghith, J.P. Corriou, Convective heat and mass transfer with evaporation of a falling film in a cavity, Int. J. Therm. Sci. 45 (2006) 16–28.
[25] D. Lakehal, M. Meier, M. Fulgosi, Interface tracking towards the direct simulation of heat and mass transfer in multiphase flows, Int. J. Heat Fluid Flow 23 (2003) 242–257.
[26] W. Murgatroyd, The role of shear and form forces in the stability of a dry patch in two-phase film flow, Int. J. Heat Mass Transfer 8 (1965) 297–301.
[27] T. Fujita, T. Ueda, Heat transfer to falling liquid films and film breakdown-I (Subcooled liquid films), Int. J. Heat Mass Transfer 21 (1978) 97–108.
[28] O.A. Kabov, Breakdown of a liquid film flowing over the surface with a local heat source, Thermophys. Aeromech. 7 (4) (2000) 513–520.
[29] A. Oron, S.H. Davis, S.G. Bankoff, Long-scale evolution of thin liquid films, Rev. Mod. Phys. 69 (3) (1997) 931–980.
[30] O.A. Kabov, Yu.V. Lyulin, I.V. Marchuk, D.V. Zaitsev, Locally heated shear-driven liquid films in microchannels and minichannels, Int. J. Heat Fluid Flow 28 (2007) 103–112.
[31] O.A. Kabov, J.C. Legros, I.V. Marchuk, B. Scheid, Deformation of the free surface in a moving locally-heated thin liquid layer, Fluid Dyn. 36 (3) (2001) 521–528.
[32] M.D. Mikhailov, General solutions of the heat equation in finite regions, Int. J. Eng. Sci. 10 (7-A) (1972) 577–591.
[33] V.S. Vladimirov, Equations of Mathematical Physics, Nauka, Moscow, 1981 (in Russian).
[34] D.V. Zaitsev, O.A. Kabov, A.R. Evseev, Measurement of locally heated liquid film thickness by a double-fiber optical probe, Exp. Fluids 34 (6) (2003) 748–754.
[35] R.C. Reid, J.M. Prausnitz, T.K. Sherwood, The Properties of Gases and Liquids, McGraw-Hill, New York, 1981.
[36] G. Hetsroni, A. Mosyak, E. Pogrebnyak, L.P. Yarin, Heat transfer in micro-channels: comparison of experiments with theory and numerical results, Int. J. Heat Mass Transfer 48 (2005) 5580–5601.
[37] G. Gimbutis, Heat Transfer in Gravitational Liquid Film Flow, Moksklas, Vilnius, 1988.
[38] I.V. Marchuk, O.A. Kabov, Numerical simulation of heat transfer in a falling liquid film with allowance for heat conduction in heaters, Russian J. Eng. Thermophys. 10 (2) (2000) 147–165.
[39] V.S. Ajaev, Spreading of thin volatile liquid droplets on uniformly heated surface, J. Fluid Mech. 528 (2005) 279–296.